APL Photonics

On-chip fluorescence detection using photonic bandgap guiding optofluidic hollow-core light cage

Cite as: APL Photonics **7**, 106103 (2022); https://doi.org/10.1063/5.0102071
Submitted: 06 June 2022 • Accepted: 12 September 2022 • Accepted Manuscript Online: 12 September 2022 • Published Online: 06 October 2022

Jisoo Kim, Bumjoon Jang, Torsten Wieduwilt, et al.

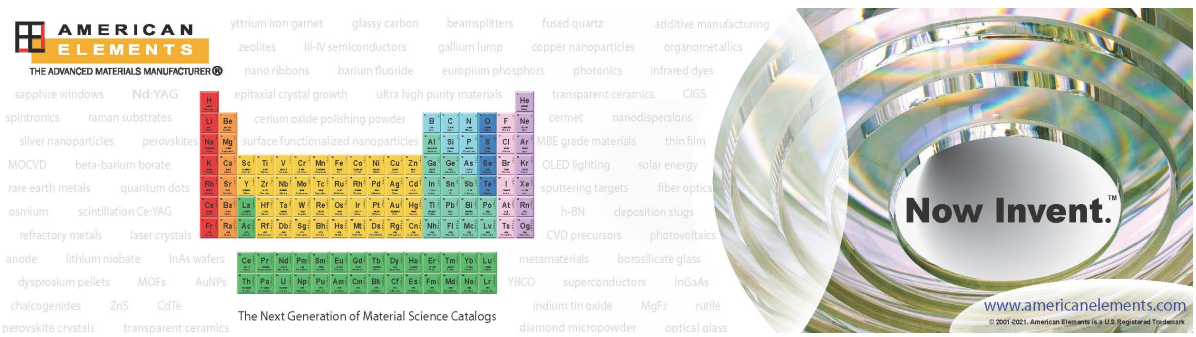

AIP Publishing

On-chip fluorescence detection using photonic bandgap guiding optofluidic hollow-core light cage

Cite as: APL Photon. 7, 106103 (2022); doi: 10.1063/5.0102071
Submitted: 6 June 2022 • Accepted: 12 September 2022 •
Published Online: 6 October 2022

Jisoo Kim,[1,2] Bumjoon Jang,[1,2] Torsten Wieduwilt,[1] Stephen C. Warren-Smith,[3] Johannes Bürger,[4] Stefan A. Maier,[4,5,6] and Markus A. Schmidt[1,2,7,a)]

AFFILIATIONS

[1] Leibniz Institute of Photonic Technology, Albert-Einstein-Str. 9, 07745 Jena, Germany
[2] Abbe Center of Photonics and Faculty of Physics, Friedrich-Schiller-University Jena, Max-Wien-Platz 1, 07743 Jena, Germany
[3] Future Industries Institute, University of South Australia, Mawson Lakes, SA 5095, Australia
[4] Chair in Hybrid Nanosystems, Nanoinstitute Munich, Ludwig-Maximilians-Universität Munich, 80799 Munich, Germany
[5] The Blackett Laboratory, Department of Physics, Imperial College London, London SW7 2AZ, United Kingdom
[6] School of Physics and Astronomy, Monash University, Clayton Campus, VIC 3800, Australia
[7] Otto Schott Institute of Materials Research (OSIM), Friedrich Schiller University Jena, Fraunhoferstr. 6, 07743 Jena, Germany

[a)] **Author to whom correspondence should be addressed:** markus.schmidt@leibniz-ipht.de

ABSTRACT

The on-chip detection of fluorescent light is essential for many bioanalytical and life-science related applications. Here, the optofluidic light cage consisting of a sparse array of micrometer encircling a hollow core represents an innovative concept, particularly for on-chip waveguide-based spectroscopy. In the present work, we demonstrate the potential of the optofluidic light cage concept in the context of integrated on-chip fluorescence spectroscopy. Specifically, we show that fluorescent light from a dye-doped aqueous solution generated in the core of a nanoprinted dual-ring light cage can be efficiently captured and guided to the waveguide ports. Notably, the fluorescence collection occurs predominantly in the fundamental mode, a property that distinguishes it from evanescent field-based waveguide detection schemes that favor collection in higher-order modes. Through exploiting the flexibility of waveguide design and 3D nanoprinting, both excitation and emission have been localized in the high transmission domains of the fundamental core mode. Fast diffusion, detection limits comparable to bulk measurements, and the potential of this approach in terms of device integration were demonstrated. Together with previous results on absorption spectroscopy, the achievements presented here suggest that the optofluidic light cage concept defines a novel photonic platform for integrated on-chip spectroscopic devices and real-time sensors compatible with both the fiber circuitry and microfluidics. Applications in areas such as bioanalytics and environmental sciences are conceivable, while more sophisticated applications such as nanoparticle tracking analysis and integrated Raman spectroscopy could be envisioned.

I. INTRODUCTION

Fluorescence detection represents a wide-spread technology particularly within bioanalytics and is used in a great variety of applications, such as medical diagnostics,[1] quantitative polymerase chain reaction (PCR) test with fluorescence,[2] fluorescence enzyme-linked immunosorbent assay (ELISA),[3] fluorescence resonance energy transfer (FRET) assay,[4] and fluorescence imaging.[5] Emerging nanotechnologies are extending the range and capabilities of applications that exploit fluorescence emission, such as super-resolution microscopy using up-conversion nanoparticles[6] and magnetic field sensing using the fluorescence emission properties of nitrogen-vacancy centers in nano-diamonds.[7] Fluorescence detection has also been used in the context of the current SARS-CoV-2 pandemic. Here, qPCR testing, with fluorescence-based detection, is considered

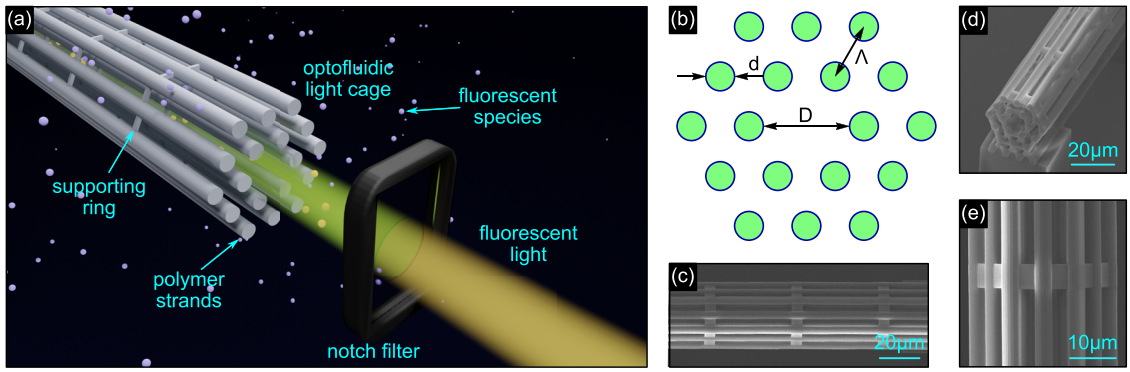

FIG. 1. Fluorescence detection in the optofluidic dual-ring light cage. (a) Illustration of the optofluidic light cage and fluorescence light. (b) Schematic of the cross section of the dual-ring light cage with the relevant geometric parameters (light green: polymer). (c)–(e) Various scanning electron microscopy (SEM) images of the dual-ring light cage used in the presented experiments [(c) top view; (d) tilted front view; (e) closed-up view of the strands].

the gold standard, and there are advantages in sensitivity in using fluorescence-based antigen/antibody tests.[8]

The excitation and collection mechanism used in a fluorescence-based system has a significant impact on the performance of the technology. A promising way to improve the performance relies on enhancing the light–matter interaction through on-chip waveguides[9] in combination with optical fibers.[10] One widely used detection scheme uses the optical evanescent field whereby a fluorescent particle can be excited and the emission can be collected through an evanescent field interaction. The advantage of this method is that the signal can be collected over long interaction lengths, with one example being the detection of single nano-crystals in microstructured fibers.[11–13] However, evanescent field detection as a reliable technology for real-world use is challenging due to limitations such as spatially restricted light–matter interaction only near the waveguide, limited fraction of the optical field in the medium of interest, potential surface contamination, background signals (fluorescence and Raman) from the waveguide material itself, dependence of the mode field on wavelength, and appearance of chromatography effects.

One promising waveguide system with particularly relevant properties for spectroscopic applications allowing one to circumvent the mentioned issues is on-chip hollow-core waveguides. Different from solid-core systems, these waveguides allow guiding light in a medium with a refractive index (RI) lower than the cladding and offer almost 100% overlap of the guided mode with the material of interest. In the majority of cases, on-chip hollow-core waveguide-based fluorescence detection relies on anti-resonant reflecting optical waveguides (ARROWs)[14] with applications including biosensors,[15] quantum dot fluorescence detection,[16] and UV fluorescence detection.[17] Note that hollow-core fibers also are successfully employed for fluorescence detection, examples of which include photonic bandgap (PBG) fibers[18,19] and anti-resonance fibers.[20] In addition to increased optical overlap with the fluorophore of interest, hollow-core waveguides have a secondary advantage that the overlap with the waveguide material is dramatically reduced, thus reducing the background autofluorescence. This advantage is particularly pronounced for weak signals such as the detection of Raman scattering using liquid or gas filled hollow-core optical fibers.[21,22]

Even though being successfully employed, today's hollow-core waveguides reveal limitations such as limited access to the waveguide core only through the open ends, leading to very long diffusion times (e.g., for low-pressure atomic gases, this can be months to fill a fiber over a length of several centimeters[23]). Moreover, interfacing on-chip hollow-core waveguides with fiber circuitry and complex fabrication schemes (e.g., ARROWs rely on the electron beam lithography with nano-film deposition) remain key challenges.

The authors have recently introduced the concept of the on-chip hollow-core light cage.[24–26] This structure consists of a spare array of dielectric strands surrounding a central hollow section acting as the waveguide core. This structure is particularly interesting for integrated spectroscopy {i.e., for integrated quantum optics [electromagnetically-induced-transparency (EIT)[27]]} as it uniquely provides an open space between the strands allowing for efficient diffusion of species into the core in contrast to the tube-type hollow waveguides introduced above and can be interfaced with fiber circuitry.[28]

We have recently extended the light cage concept toward microfluidics, demonstrated by absorption spectroscopic experiments of light cages immersed in dye solutions.[29] Together with the recent gas-related experiments,[28] these results reveal the potential of the light cage concept regarding spectroscopic applications.

In this work, we evaluate the optofluidic light cage concept regarding an integrated on-chip fluorescence-based spectroscopy [Fig. 1(a)]. Through immersing the light cage into dye-doped aqueous solution, we show that the fluorescent light is efficiently captured and guided to the waveguide's output. Using the flexibility of the light cage geometry, we show that both excitation and emission wavelengths can be placed into the PBG regions (high transmission domains) of the fundamental core mode. By using Rhodamine B dissolved in water, detection limits that match corresponding bulk fluorescence measurements are presented.

II. EXPERIMENTAL

The fundamental idea of the presented study relies on using the PBG effect to efficiently capture and guide the fluorescence light,[18] requiring a periodic arrangement of a dielectric material.[30] Such an

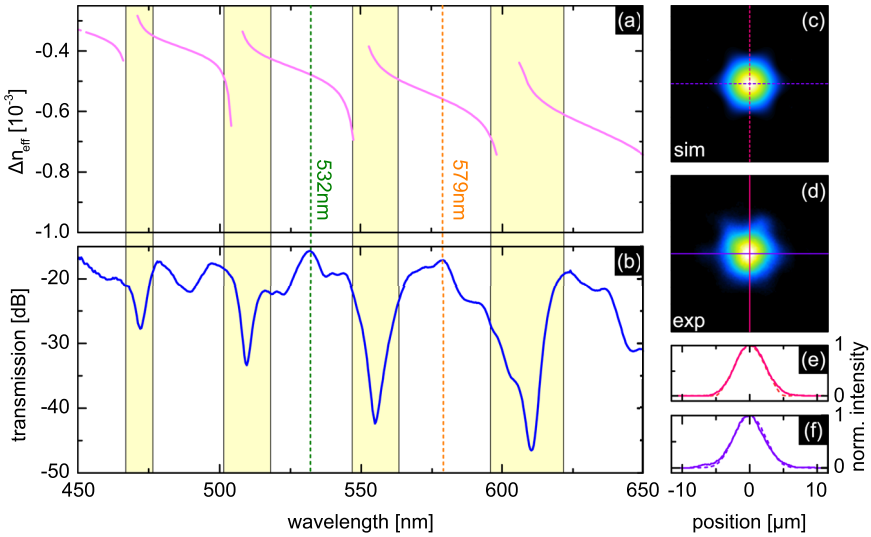

FIG. 2. Optical properties of the dual-ring optofluidic light cage. (a) Simulated relative effective index Δn_{eff} of the fundamental leaky core mode across the spectral domain of interest. The green and orange dashed lines indicate the excitation and the main emission wavelengths used in the experiments. (b) Corresponding transmission measurements. The yellow areas refer to the domains of high loss corresponding to the domains of the resonances. (c) Simulated Poynting vector distribution of the fundamental light cage mode at λ = 532 nm (linear scale, white: unity, dark: zero). (d) Measured output mode pattern in case white light is launched into the optofluidic light cage. The curves shown in (e) and (f) refer to the intensity distributions along the lines indicated in (c) and (d) (solid: experiments, dashed: simulations).

arrangement is provided by the optofluidic light cage [Fig. 1(a)] consisting of a hexagonal array of dielectric strands [cross section shown in Figs. 1(b) and 1(d) = 3.6 μm, Λ = 7 μm, and D = 14 μm]. The core is formed by the omitted central strand and supports a leaky mode through the PBG effect.[31,32] Note that the PBG effect results from the interference of waves scattered by the various elements, leading to resonances in the dispersion of the fundamental core mode [Fig. 2(a), material dispersion of polymer and water can be found in Ref. 29]. Here, modal dispersion is represented by the relative effective index $\Delta n_{eff} = n_{eff} - n_{water}$ (n_{eff}: effective mode index and n_{water}: refractive index of water). The resonances match the high loss domains [Fig. 2(b)] of the measured transmission spectrum [yellow areas in Figs. 2(a)–2(b), details of the measurements are explained later in the text], while high transmission is obtained in-between the resonances. Remarkably, resonances with large fringe contrast (on-off power ratio >25 dB) are measured, being comparable to values obtained in all-solid PBG fibers.[31,33] Note that this large contrast is a result of the presence of the second ring, improving the light guidance properties of the device through stronger light confinement.[25] Such pronounced resonances indicate strong core mode formation overall resulting from the use of two rings of strands.

Here, we would like to highlight that the power fraction within the core is greater than 99% in the middle of the transmission bands [simulated and measured mode patterns at λ = 532 nm are shown in Figs. 2(c) and 2(d)], whereby the strands only occupy a fraction of the cladding area. Note that the measured and simulated mode profiles match to a very high degree as visible by the quantitative comparison of the spatial intensity distributions shown in Figs. 2(e) and 2(f). Another remarkable feature is that the design freedom of the light cage geometry allows us to localize both the excitation (λ = 532 nm, green dashed lines in Figs. 2 and 3) and the emission wavelength (λ = 579 nm, orange dashed lines in Figs. 2 and 3) within high transmission regions, which was achieved through adjusting the strand diameters. As mentioned in Ref. 34, this spectral tuning was achieved through adjusting the strand diameters, allowing one to shift the cut-offs of the isolated strand modes and, thus, the resonances. Therefore, the light cage allows for both guiding the excitation light to the fluorescent molecules and efficiently capturing the uniformly emitted fluorescent light.

As shown in Refs. 26 and 34, light cages with losses on the order of 0.5 dB/mm < γ < 1 dB/mm at visible wavelengths can be realized with the current fabrication approach with the maximum length of light cage implemented so far being 30 mm.[34] Taking into account this loss figure and the size of our liquid chamber, we choose a light cage length of L = 4.5 mm for the experiments presented here.

As an example dye we chose Rhodamine B (RhoB, molar mass: 479.01 g/mol) dissolved in water. Two concentration ranges corresponding to a low (0.075μM < c < 2.4 μM) and a high (3.75μM < c < 30 μM) dye concentration were used. The solutions were characterized using an in-house spectrometer (F550B from Perkin Elemer), which showed that maximum excitation and emission (for c = 1 μM) occurs at λ = 552.6 nm and λ = 576.5 nm, respectively (details in the supplementary material). It is important to mention that the maximum of the emission red-shifts for increasing c, an effect that we attribute to dimer formation[35,36] (Fig. SI3). Here, we assume that the maximum emission is located at λ = 579 nm, which holds in the low concentration regime up to c = 2.4 μM.

The dual-ring light cages were fabricated by nanoprinting using a commercial 3D lithography system (Photonic Professional GT2, Nanoscribe GmbH, details in the supplementary material). Before printing, the surface of the silicon substrates was exposed to a silanization step to increase the adhesion of the polymer structure to the silicon.[37] To prevent structural collapse during development, the strands were supported and interconnected every 30 μm by

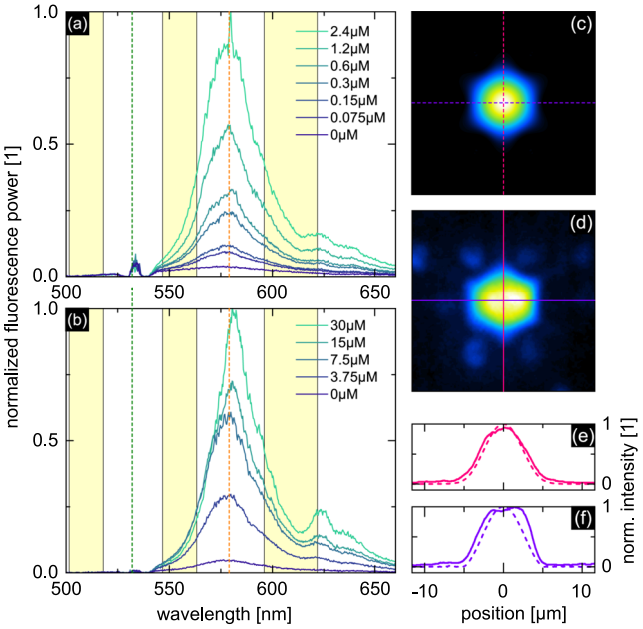

FIG. 3. Measured fluorescence collection properties enabled by the optofluidic light cage, demonstrated using the example of RhoB dissolved in water. (a) and (b) Fluorescence collection properties of the dual-ring optofluidic light cage [(a) low concentration regime ($0 < c < 2.4\ \mu$M) and (b) high concentration regime ($0 < c < 30\ \mu$M)]. The yellow areas refer to the domains of high loss regions shown in Figs. 2(a) and 2(b). The curves have been normalized to the highest value in the respective plot. (c) Simulated Poynting vector distribution of the core mode at $\lambda = 579$ nm (linear scale, white: unity, dark: zero). (d) Measured output mode in case the excitation light at 532 nm is filtered out, thus solely corresponding to the collected fluorescence light ($c = 30\ \mu$M). The curves shown in (e) and (f) refer to the intensity distributions along the lines indicated in (c) and (d) (solid: experiments, dashed: simulations). The curves shown in (e) and (f) refer to the intensity distributions along the lines indicated in (c) and (d) (solid: experiments, dashed: simulations).

reinforcement rings. The supporting elements have been designed to have no significant impact on the optical properties of the light cage as shown in Refs. 29 and 34 and in the supplementary material. This observation is supported by additional modal overlap simulations of the modes of the cross sections with and without the supporting elements, showing close-to-unity values for all possible combinations of cross sections and, thus, proving the negligible impact of the elements. To conduct the optical experiments, the silicon chips with the light cages were fixed inside a home-made optofluidic chamber (volume 300 μl, details in the supplementary material, Fig. SI1). This chamber allows for launching and collecting the light signals through glass windows and dye insertion without light cage removal.

To carry out the various experiments, the setup for the optical characterization was modular and relied on a combination of a suitable light source, the light cages located in the fluidic chamber and spectral diagnostics and cameras. Excitation of the fundamental light cage mode and light collection at the output side was achieved through suitable objectives (a sketch of the experimental setup together with further details is shown in Fig. SI2). The transmitted signal was either guided via a multimedia fiber to the spectrometers or imaged via cameras.

For the broadband characterization [Fig. 2(b)], a commercially available supercontinuum source (SuperK COMPACT, NKT Photonics) and an optical spectrum analyzer (AQ-6315A, Ando, spectral resolution used: $\Delta\lambda = 0.4$ nm) were employed. The setup was optimized for maximum throughput, i.e., for the situations where the fundamental core mode is the brightest. The transmission spectra were normalized by using a spectrum measured without a light cage.

In the case of the fluorescence measurements (Fig. 3), the fundamental core mode was excited with a narrowband diode laser (W532-50FS, Pavilion Integration Corp., $\lambda = 532$ nm, maximal power 50 mW). The output light was detected using a fast spectrometer (USB2000, Ocean insight, 450 nm $< \lambda <$ 800 nm, $\Delta\lambda = 0.32$ nm), while a notch filter (blocking range 523 nm $< \lambda <$ 544 nm, extinction ratio < -20 dB, OD = 6 @ 533 nm) was inserted into the beam path to prevent the residual excitation light reaching the detection system.

The fluorescence-related experiments rely on measuring the collected light power spectrally resolved for different concentrations at the same input power level. As mentioned above, two types of concentration ranges were addressed, while a starting concentration (high range: $c = 30\ \mu$M and low range $c = 2.4\ \mu$M) was successively diluted by adding water. The integration time of the spectrometer was different in the two studies and was adjusted via different attenuation filters to maximize the signal on the spectrometer before reaching saturation at the initial concentration. The integration time within one concentration range remained unchanged to allow for qualitatively comparing the fluorescence data.

III. RESULTS AND DISCUSSION

The mode pattern of the fluorescence measurements [Fig. 3(d)] shows a sixfold symmetry that resembles the corresponding simulated pattern of the fundamental mode [Fig. 3(c)]. The quantitative comparison of the intensity distributions [Figs. 3(e) and 3(f)] confirms this observation, while a slightly broader distribution of the measured profile particularly in the horizontal direction (purple lines) is observed, indicating a small contribution from higher-order modes. This intensity distribution, which is also observed for other concentrations, confirms the efficient collection and transportation of the fluorescence light to the output of the dual-ring light cage mainly through the fundamental mode. This particular feature distinguishes the light cage concept from evanescent field-related schemes, which show higher collection efficiency for the higher-order modes, allowing for simpler outcoupling to detection optics. Note that the high fundamental mode capturing efficiency results from the strong modal overlap between the fundamental modes at the excitation and fluorescence wavelengths. Only a small fraction of overall electromagnetic power recorded was located in the strands and, therefore, we consider that the fluorescent light captured and guided by the strands is negligible. The fluorescence power guided to the output increases with dye concentration [Figs. 3(a) and 3(b), at a constant input power ($P_{in} = 14$ mW after attenuation)], with the emission peaking at roughly $\lambda = 579$ nm as expected. Note that for the high concentrations [Fig. 3(b)], a spectral red-shift of the fluorescence maximum is observed, which in accordance with bulk measurements [examples of emission spectra at two selected concentrations (low and high) are shown in Figs. SI3(a) and SI3(b)] can be explained by the dimer formation.[35] The spectral fingerprint of the light cage is visible in the emission spectra, in particular for high

dye concentrations [Fig. 3(b)]: A reduction in fluorescence occurs when the spectral domains of high modal attenuation (yellow area in Fig. 3(b)) overlap with the fluorescence spectrum. This effect is particularly pronounced for 600 nm < λ < 620 nm in the case of high dye concentration [e.g., cyan curve in Fig. 3(b)]. Note that the small peaks for 530 nm < λ < 535 nm visible in Figs. 3(a) and 3(b) result from the residual excitation light passing through the notch filter and not from the residual fluorescent light of the dye, which is evident from the fact that the amplitude of this peak does not change with dye concentration. The constant residual pump light visible in Figs. 3(a) and 3(b) confirms operation in the linear absorption regime, i.e., that the device does not suffer from pump depletion. Therefore, the sensor output will respond linearly as expected.

We would like to mention that in the case of pure water (c = 0), photoluminescence from the polymer strand can be measured (Fig. SI5). The detection of this radiation requires setting the integration times of the spectrometer to much higher values than used in the actual fluorescence experiments, preventing the detection of this residual light in the experiments.

For a quantitative assessment of the light cage properties, we analyzed the fluorescence power (normalized to the power at c = 2.4 μM) as a function of concentration at the main fluorescence wavelength (λ = 579 nm) for both the light cage and cuvette-based measurements, finally yielding the limit-of-detections (LoDs). Please note that we decided to analyze the low concentration regime (0 < c < 1.2 μM), which does not show a red-shift of the main absorption line with concentration. The resulting plots [Figs. 4(a) and 4(b)] show linear dependencies in both cases, which are fitted by linear functions $\Delta P(c) = m \cdot c + P_0$ (m: slope, ΔP_0: normalized offset power) to obtain the calibration relations (light cage: m = 0.76074 $\mu m^{-1}M^{-1}$, ΔP_0 = 0.117 31; cuvette: m = 0.762 33 $\mu m^{-1}M^{-1}$, ΔP_0 = 0.029 69). For both cases, a linear behavior with the same slope is obtained, suggesting a direct application of the light cage concept in fluorescence-related experiments without the involvement of modal calculation. Note that this effect results from the close-to-unity fraction of power in the core (absorption wavelength: 99.2% and emission wavelength: 99.6%). The slight deviations of the data points from a purely linear behavior can be attributed to unavoidable experimental circumstances, such as noise and error in preparing the concentration samples. Note that the behavior gets nonlinear in the high concentration regime, resulting from the mentioned spectral red-shift of the fluorescence maximum due to dimer formation (details can be found in the supplementary material, Fig. SI4).

Within the context of fluorescence spectroscopy, the LoD is defined by LoD = 3σ/m,[38] with σ being the standard deviation of the normalized power of blank measurements and m being the sensitivity found from the linear fit in Fig. 4. For both bulk and light cage measurements, the standard deviation is determined for the pure water case (c = 0), while in the light cage situations, this additionally includes the photoluminescence of the polymer strands being present at any dye concentration. The resulting LoD in the case of the light cage is LoD_{lc} = 8 nM, matching the value from the bulk cuvette measurements (LoD_c = 10 nM).

An essential feature of the optofluidic light cage is the lateral access to the core domain, a property that conventional hollow-core waveguides with capillary-like geometries do not have. This property is particularly important for the analysis of diffusion processes and is demonstrated below by the time-resolved collection of the fluorescent light (Fig. 5). Specifically, the power of the core mode at the main fluorescence wavelength (λ = 527 nm) is continuously monitored when a certain amount of dye is introduced into the water-filled chamber (details can be found in the supplementary material). The results are compared to a fiber-type capillary of identical core parameters showing a fast increase in the collected fluorescent power for the light cage, reaching 99% of the maximal power in about 8 min ($t_{99\%}$ = 500 s, green dots in Fig. 5).

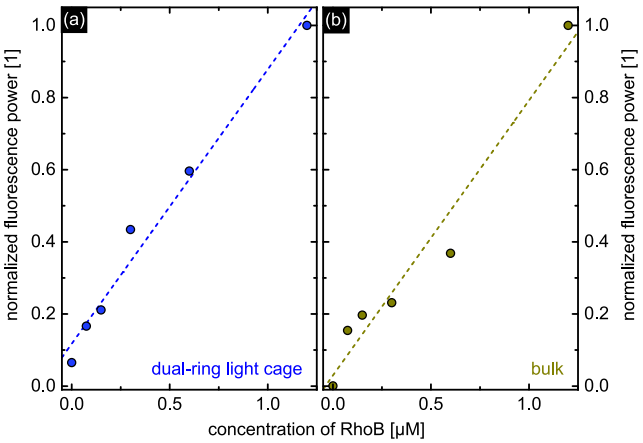

FIG. 4. Quantitative analysis of the fluorescence properties. Measured fluorescence power/concentration relation at the main fluorescence line (λ = 579 nm, yellow lines in Figs. 2 and 3). (a) Dual-ring light cage. (b) Cuvette-based reference measurement. The dots correspond to the measured data, while the lines refer to the linear fits.

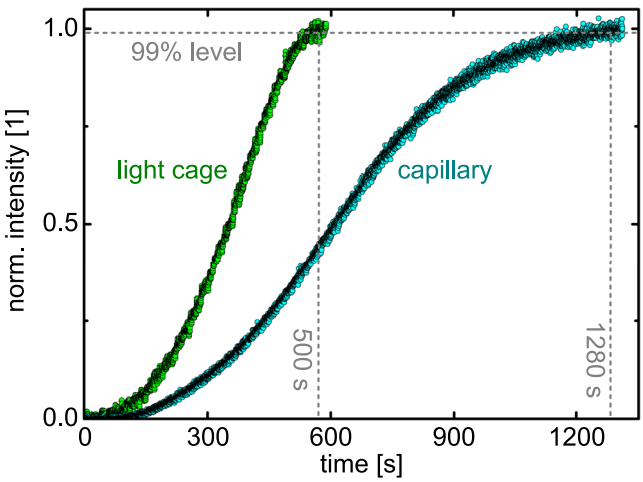

FIG. 5. Dynamic behavior of the fluorescence power (normalized to maximum value) collected by the dual-ring optofluidic light cage (green) in comparison to a fiber-type capillary with comparable core diameter (cyan, core diameter D = 15 μm) at a main emission wavelength (λ = 579 nm). Identical chambers and lengths (L = 5 mm) are used. The horizontal gray dashed line refers to 99% of the saturated power.

TABLE I. Fluorescence-related capabilities of the optofluidic light cage in relation to reported results from integrated waveguide systems.

Type of waveguide	Device length	Core diameter	Dye	Demonstrated concentration	Limit of detection	Reference
Dual-ring light cage	4.5 mm	14 μm	Rhodamine B	75 nM	8 nM	This work
Solid core microstructured optical fibers (SC-MOFs)	10 cm	3.7 μm (cladding hole)	Rhodamine 6G	1 μM	1 μM	18
Hollow-core photonic crystal fibers (HC-PCFs)	10 cm	5.3 μm (central core)	Rhodamine 6G	0.1 nM	0.1 nM	18
Suspended core microstructured optical fibers (SCFs)	25 cm	1.38 μm (core)	Rhodamine B	10 nM	N.A	13
Poly vinyl pyrrolidone and poly vinyl alcohol waveguide	N.A	N.A	Rhodamine B	1 μM	N.A	39
Dye doped PMMA waveguide	1.2 cm	(120 × 1) μm	Rhodamine 640	20 μM	N.A	40
Doped polymer film waveguide	2.4 cm	1.5 mm beam size	Rhodamine 6G	100 μM	N.A	41
Metal coated strip waveguide	1.5 cm	20 μm	Rhodamine B	1.04 μM	N.A	42

This suggests a much faster diffusion compared to other hollow-core waveguides, as about 2.6 times longer diffusion times for the capillary ($t_{99\%}$ = 1280 s, green dots in Fig. 5) are measured.

To classify the properties, the obtained results of the optofluidic light cage are compared to other waveguide-based fluorescence experiments in Table I. Clearly visible is that the optofluidic light cage allows for fluorescence-based detection of very small dye concentrations and has an overall small LoD. The only systems with smaller LoD-numbers are hollow-core fibers and suspended core fibers, both of which use fibers of substantially longer length which do not provide sidewise access. Note that in a recent study,[34] we have been able to experimentally demonstrate a very high reproducibility of the light cage concept by a statistical analysis.

Increasing the length of the light cage represents one pathway to enhance the amount of captured fluorescence power. Here, recent experiments have shown that the maximal length of the light cage that can be realized with the current nanoprinting scheme is 30 mm.[34] While such a long length suggests an improved collection performance, modal attenuation of 0.5 dB/mm < γ < 1 dB/mm limits the total device length. Another pathway for enhancing the device performance is to reduce the core size to increase capturing efficiency of the fundamental mode,[11] requiring strands of smaller diameter and in particular smaller pitch values.

One important feature of the optofluidic light cage concept is the opportunity to spectrally tune the high transmission bands. This flexibility allows us to simultaneously match the excitation and emission wavelengths with the high transmission regions, which is achieved here by tuning the dispersion of the strand modes. Extending the number of degrees of tunability can be realized by either changing the shape of the strands (e.g., elliptical, square, or rectangular) or through functionalizing the strands by photonic elements (e.g., nano-films[24]). We recently demonstrated dielectric strands with significantly smaller diameters (<1.5 μm) leading to wider transmission regions. This may allow for creating broadband transmission windows that include both the excitation and emission wavelengths.

The optofluidic light cage concept includes a great potential for device integration, e.g., within the context of fiber circuitry. Here, we have recently demonstrated the successful interfacing of commonly used step-index fibers and light cages through v-grooves on silicon chips,[28] showing coupling efficiencies between fiber and cage of the order of 80%. The capabilities within this context of gas-related spectroscopy have been revealed through a laser-scanning absorption spectroscopic experiment for the integrated detection of ammonia. This idea was applied in this work for realizing fiber-interfaced optofluidic light cages: Here, cages were nanoprinted in-between aligned single-mode and multi-mode fibers (SMFs and MMFs) for light delivery and collection, respectively (Fig. 6), all of

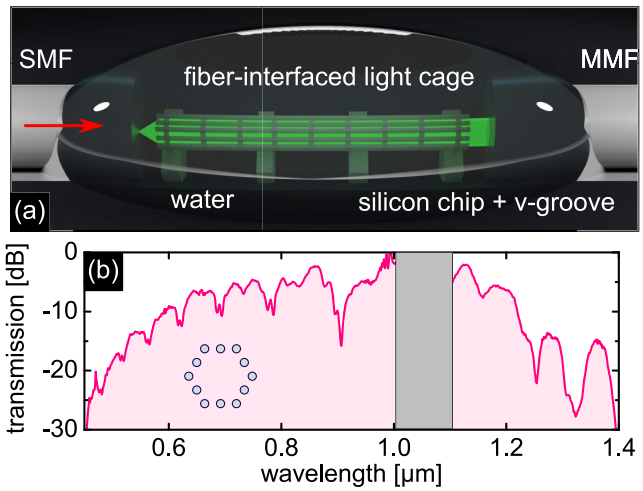

FIG. 6. (a) Illustration of a fiber-interfaced single-ring light cage located on a silicon chip that includes v-grooves for auto-alignment (red arrow: direction of the light). (b) Corresponding measured transmission spectrum normalized to the maximum value. Light between 1 and 1.1 μm (gray area) has been filtered out to prevent heating (details in the supplementary material). The inset show the cross section of the light cage used.

which are immersed in water (details in the supplementary material). The corresponding transmission spectrum (Fig. 6) shows the characteristic features of anti-resonance guidance (alternating high and low transmission), verifying the operation principle and emphasizing the potential of the optofluidic light cage concept regarding device integration. Note that the same type of fiber and light cage was used as in Ref. 28, so coupling coefficients in the range of 80% between fiber and light cage can be expected.

IV. CONCLUSIONS

The integrated and efficient detection of fluorescent light using a compact device is essential for many bioanalytical applications. In this regard, the optofluidic light cage represents an innovative concept that has the potential to circumvent limitations of currently used waveguide devices. In this work, we investigate and evaluate the optofluidic light cage concept in the context of integrated on-chip fluorescence spectroscopy. Specifically, we show that fluorescent light from a dye-doped aqueous solution generated in the core of a dual-ring light cage can be efficiently captured and guided to the waveguide ports. As experimentally demonstrated, the flexibility of the light cage design and of the 3D nanoprinting process allows for localization of both the excitation and emission within the high transmission domains of the fundamental core mode. Detection limits for Rhodamine 6G that match bulk measurements, fast dye diffusion, and the potential of the concept for interfacing with fiber circuitry have been revealed experimentally. One feature worth highlighting is the collection of fluorescent light predominantly in the fundamental mode, a feature that distinguishes it from evanescent field-related waveguide detection schemes that favor collection in higher-order modes. In combination with previous results on absorption spectroscopy and implementation reproducibility, the results presented here suggest that the optofluidic light cage concept represents a novel photonic platform with great potential for integrated spectroscopy compatible with fiber circuits, on-chip approaches, and microfluidics. Applications in areas such as bioanalytics and environmental sciences are conceivable, while more sophisticated applications such as nanoparticle tracking analysis or Raman spectroscopy could be targets of future research. The possibilities of the light cage concept are not limited to a single species, and the acquisition of fluorescence signals from multiple emitting species is conceivable. Therefore, the optofluidic light cage offers a promising new direction for the use of hollow-core waveguides in laboratory-on-a-chip applications, combining high-efficiency fluorescence detection with integrated microfluidics. Future improvements in the yield and throughput of nanoprinting technology could enable large-scale implementation, as the optofluidic light cage itself has a small geometric footprint and physically requires very little material.

SUPPLEMENTARY MATERIAL

See the supplementary material for more details on the impact of supporting elements, light cage implementation, optofluidic chamber, experimental setup, spectral properties of the dye solution, fluorescence within the high concentration regime, autofluorescence of polymer, dynamic measurements, and fiber-interfaced light cage.

ACKNOWLEDGMENTS

This work was supported by funding from the Deutsche Forschungsgemeinschaft (Grant Nos. SCHM2655/15-1, SCHM2655/11-1, SCHM2655/8-1, MA4699/2-1, and Germany's Excellence Strategy—EXC 2051—Project-No. 390713860) and Lee-Lucas Chair in Physics (Imperial College London, UK).

AUTHOR DECLARATIONS

Conflict of Interest

The authors have no conflicts to disclose.

Author Contributions

Jisoo Kim: Conceptualization (supporting); Data curation (lead); Formal analysis (lead); Investigation (lead); Methodology (lead); Resources (lead); Software (lead); Validation (supporting); Visualization (lead). **Bumjoon Jang**: Data curation (supporting); Formal analysis (supporting); Investigation (supporting). **Torsten Wieduwilt**: Investigation (supporting); Methodology (supporting); Resources (supporting). **Stephen C. Warren-Smith**: Data curation (supporting); Formal analysis (supporting). **Johannes Bürger**: Conceptualization (supporting); Formal analysis (supporting); Investigation (supporting). **Stefan A. Maier**: Conceptualization (equal); Project administration (supporting); Supervision (supporting); Validation (supporting); Visualization (supporting). **Markus A. Schmidt**: Conceptualization (equal); Data curation (supporting); Formal analysis (supporting); Funding acquisition (lead); Investigation (supporting); Methodology (supporting); Project administration (lead); Resources (supporting); Software (supporting); Supervision (lead); Validation (equal); Visualization (supporting).

DATA AVAILABILITY

The data that support the findings of this study are available from the corresponding author upon reasonable request.

REFERENCES

[1] A. Shahzad, M. Knapp, M. Edetsberger, M. Puchinger, E. Gaubitzer, and G. Köhler, "Diagnostic application of fluorescence spectroscopy in oncology field: Hopes and challenges," Appl. Spectrosc. Rev. **45**, 92–99 (2010).
[2] J. Cheong, H. Yu, C. Y. Lee, J. U. Lee, H. J. Choi, J. H. Lee, H. Lee, and J. Cheon, "Fast detection of SARS-CoV-2 RNA via the integration of plasmonic thermocycling and fluorescence detection in a portable device," Nat. Biomed. Eng. **4**, 1159 (2020).
[3] J. R. Lakowicz, *Principles of Fluorescence Spectroscopy* (Springer Science & Business Media, 2013).
[4] M. A. Rizzo, G. H. Springer, B. Granada, and D. W. Piston, "An improved cyan fluorescent protein variant useful for FRET," Nat. Biotechnol. **22**, 445–449 (2004).
[5] B. A. Flusberg, E. D. Cocker, W. Piyawattanametha, J. C. Jung, E. L. Cheung, and M. J. Schnitzer, "Fiber-optic fluorescence imaging," Nat. Methods **2**, 941–950 (2005).
[6] Y. Liu, Y. Lu, X. Yang, X. Zheng, S. Wen, F. Wang, X. Vidal, J. Zhao, D. Liu, Z. Zhou *et al.*, "Amplified stimulated emission in upconversion nanoparticles for super-resolution nanoscopy," Nature **543**, 229–233 (2017).
[7] D. Bai, M. H. Huynh, D. A. Simpson, P. Reineck, S. A. Vahid, A. D. Greentree, S. Foster, H. Ebendorff-Heidepriem, and B. C. Gibson, "Fluorescent diamond

microparticle doped glass fiber for magnetic field sensing," APL Mater. **8**, 081102 (2020).
[8]D. Wang, S. He, X. Wang, Y. Yan, J. Liu, S. Wu, S. Liu, Y. Lei, M. Chen, L. Li *et al.*, "Rapid lateral flow immunoassay for the fluorescence detection of SARS-CoV-2 RNA," Nat. Biomed. Eng. **4**, 1150 (2020).
[9]Z. Liao, Y. Zhang, Y. Li, Y. Miao, S. Gao, F. Lin, Y. Deng, and L. Geng, "Microfluidic chip coupled with optical biosensors for simultaneous detection of multiple analytes: A review," Biosens. Bioelectron. **126**, 697–706 (2019).
[10]Y. Zhao, X.-g. Hu, S. Hu, and Y. Peng, "Applications of fiber-optic biochemical sensor in microfluidic chips: A review," Biosens. Bioelectron. **166**, 112447 (2020).
[11]S. Afshar V, S. C. Warren-Smith, and T. M. Monro, "Enhancement of fluorescence-based sensing using microstructured optical fibres," Opt. Express **15**, 17891–17901 (2007).
[12]J. Zhao, D. Jin, E. P. Schartner, Y. Lu, Y. Liu, A. V. Zvyagin, L. Zhang, J. M. Dawes, P. Xi, J. A. Piper *et al.*, "Single-nanocrystal sensitivity achieved by enhanced upconversion luminescence," Nat. Nanotechnol. **8**, 729–734 (2013).
[13]E. P. Schartner, G. Tsiminis, M. R. Henderson, S. C. Warren-Smith, and T. M. Monro, "Quantification of the fluorescence sensing performance of microstructured optical fibers compared to multi-mode fiber tips," Opt. Express **24**, 18541–18550 (2016).
[14]D. Yin, H. Schmidt, J. P. Barber, and A. R. Hawkins, "Integrated arrow waveguides with hollow cores," Opt. Express **12**, 2710–2715 (2004).
[15]H. Mukundan, A. Anderson, W. K. Grace, K. Grace, N. Hartman, J. Martinez, and B. Swanson, "Waveguide-based biosensors for pathogen detection," Sensors **9**, 5783–5809 (2009).
[16]J. Ozhikandathil and M. Packirisamy, "Silica-on-silicon waveguide integrated polydimethylsiloxane lab-on-a-chip for quantum dot fluorescence bio-detection," J. Biomed. Opt. **17**, 017006 (2012).
[17]P. D. Ohlsson, O. Ordeig, K. B. Mogensen, and J. P. Kutter, "Electrophoresis microchip with integrated waveguides for simultaneous native UV fluorescence and absorbance detection," Electrophoresis **30**, 4172–4178 (2009).
[18]S. Smolka, M. Barth, and O. Benson, "Highly efficient fluorescence sensing with hollow core photonic crystal fibers," Opt. Express **15**, 12783–12791 (2007).
[19]A. M. Cubillas, S. Unterkofler, T. G. Euser, B. J. M. Etzold, A. C. Jones, P. J. Sadler, P. Wasserscheid, and P. S. J. Russell, "Photonic crystal fibres for chemical sensing and photochemistry," Chem. Soc. Rev. **42**, 8629–8648 (2013).
[20]J. Yang, R. Shen, P. Yan, Y. Liu, X. Li, P. Zhang, and W. Chen, "Fluorescence sensor for volatile trace explosives based on a hollow core photonic crystal fiber," Sens. Actuators, B **306**, 127585 (2020).
[21]G. Tsiminis, K. J. Rowland, E. P. Schartner, N. A. Spooner, T. M. Monro, and H. Ebendorff-Heidepriem, "Single-ring hollow core optical fibers made by glass billet extrusion for Raman sensing," Opt. Express **24**, 5911–5917 (2016).
[22]A. Knebl, D. Yan, J. Popp, and T. Frosch, "Fiber enhanced Raman gas spectroscopy," TrAC, Trends Anal. Chem. **103**, 230–238 (2018).
[23]G. Epple, K. S. Kleinbach, T. G. Euser, N. Y. Joly, T. Pfau, P. S. Russell, and R. Löw, "Rydberg atoms in hollow-core photonic crystal fibres," Nat. Commun. **5**, 4132 (2014).
[24]B. Jang, J. Gargiulo, M. Ziegler, R. F. Ando, U. Hübner, S. A. Maier, and M. A. Schmidt, "Fine-tuning of the optical properties of hollow-core light cages using dielectric nanofilms," Opt. Lett. **45**, 196–199 (2020).
[25]B. Jang, J. Gargiulo, R. F. Ando, A. Lauri, S. A. Maier, and M. A. Schmidt, "Light guidance in photonic band gap guiding dual-ring light cages implemented by direct laser writing," Opt. Lett. **44**, 4016–4019 (2019).
[26]C. Jain, A. Braun, J. Gargiulo, B. Jang, G. Li, H. Lehmann, S. A. Maier, and M. A. Schmidt, "Hollow core light cage: Trapping light behind bars," ACS Photonics **6**, 649–658 (2018).
[27]F. Davidson-Marquis, J. Gargiulo, E. Gómez-López, B. Jang, T. Kroh, C. Müller, M. Ziegler, S. A. Maier, H. Kübler, M. A. Schmidt, *et al.*, "Coherent interaction of atoms with a beam of light confined in a light cage," Light: Sci. Appl. **10**, 114 (2021).
[28]B. Jang, J. Gargiulo, J. Kim, J. Bürger, S. Both, H. Lehmann, T. Wieduwilt, S. A. Maier, and M. A. Schmidt, "Fiber-integrated hollow-core light cage for gas spectroscopy," APL Photonics **6**, 061301 (2021).
[29]J. Kim, B. Jang, J. Gargiulo, J. Bürger, J. Zhao, S. Upendar, T. Weiss, S. A. Maier, and M. A. Schmidt, "The optofluidic light cage-on-chip integrated spectroscopy using an antiresonance hollow core waveguide," Anal. Chem. **93**, 752 (2020).
[30]M. Schmidt, M. Eich, U. Huebner, and R. Boucher, "Electro-optically tunable photonic crystals," Appl. Phys. Lett. **87**, 121110 (2005).
[31]N. Granzow, P. Uebel, M. A. Schmidt, A. S. Tverjanovich, L. Wondraczek, and P. S. J. Russell, "Bandgap guidance in hybrid chalcogenide–silica photonic crystal fibers," Opt. Lett. **36**, 2432–2434 (2011).
[32]P. S. J. Russell, "Photonic-crystal fibers," J. Lightwave Technol. **24**, 4729–4749 (2006).
[33]M. A. Schmidt, N. Granzow, N. Da, M. Peng, L. Wondraczek, and P. S. J. Russell, "All-solid bandgap guiding in tellurite-filled silica photonic crystal fibers," Opt. Lett. **34**, 1946–1948 (2009).
[34]J. Bürger, J. Kim, B. Jang, J. Gargiulo, M. A. Schmidt, and S. A. Maier, "Ultrahigh-aspect-ratio light cages: Fabrication limits and tolerances of free-standing 3D nanoprinted waveguides," Opt. Mater. Express **11**, 1046–1057 (2021).
[35]F. del Monte and D. Levy, "Formation of fluorescent rhodamine B J-dimers in sol- gel glasses induced by the adsorption geometry on the silica surface," J. Phys. Chem. B **102**, 8036–8041 (1998).
[36]K. Kemnitz, N. Tamai, I. Yamazaki, N. Nakashima, and K. Yoshihara, "Fluorescence decays and spectral properties of rhodamine b in submono-, mono-, and multilayer systems," J. Phys. Chem. **90**, 5094–5101 (1986).
[37]X. Liu, H. Gu, M. Wang, X. Du, B. Gao, A. Elbaz, L. Sun, J. Liao, P. Xiao, and Z. Gu, "3D printing of bioinspired liquid superrepellent structures," Adv. Mater. **30**, 1800103 (2018).
[38]S. E. Braslavsky, "Glossary of terms used in photochemistry, (IUPAC recommendations 2006)," Pure Appl. Chem. **79**, 293–465 (2007).
[39]S. A. Suheil, N. S. Shnan, and Q. Mohammed Salman, "The plasmon effects of AgNPs on wave guide consisting of polymers mixed with rhodamine dyes," J. Phys.: Conf. Ser. **1829**, 012007 (2021).
[40]M. C. Ramon, M. Ariu, R. Xia, D. D. C. Bradley, M. A. Reilly, C. Marinelli, C. N. Morgan, R. V. Penty, and I. H. White, "A characterization of rhodamine 640 for optical amplification: Collinear pump and signal gain properties in solutions, thin-film polymer dispersions, and waveguides," J. Appl. Phys. **97**, 073517 (2005).
[41]K. Geetha, M. Rajesh, V. P. N. Nampoori, C. P. G. Vallabhan, and P. Radhakrishnan, "Loss characterization in rhodamine 6G doped polymer film waveguide by side illumination fluorescence," J. Opt. A: Pure Appl. Opt. **6**, 379 (2004).
[42]B. H. Ong, X. Yuan, Y. Y. Tan, R. Irawan, X. Fang, L. Zhang, and S. C. Tjin, "Two-layered metallic film-induced surface plasmon polariton for fluorescence emission enhancement in on-chip waveguide," Lab Chip **7**, 506–512 (2007).